Malaysian Journal of Chemistry, 2024, Vol. 26(5), 262-272
(Special Issue: *3rd Virtual International Symposium on Sciences 2023*)

Structural and Dielectric Properties of Alkaline Earth Metal-Doped Double Perovskite Materials: A Review

Muhammad Syaabani Mohd Rafie[1], Annie Maria Mahat[2], Norazila Ibrahim[1] and Zakiah Mohamed[1]*

[1]Faculty of Applied Sciences, Universiti Teknologi MARA, 40450 Shah Alam, Selangor, Malaysia
[2]Institute of Science, Level 3, Kompleks Inspirasi, Universiti Teknologi MARA, 40450 Shah Alam, Selangor, Malaysia.
*Corresponding author (email: zakiah626@uitm.edu.my)

Due to their exceptional structural and functional features, double perovskite materials have sparked considerable interest. This review focuses on the role of alkaline earth metals as doping elements in double perovskite compounds, examining their implications on structural and dielectric properties. The review begins with an explanation of the significance of double perovskite materials in the context of advanced materials research. It then looks into the synthesis methods used to integrate alkaline earth metals as dopants in the double perovskite lattice, clarifying their impact on crystal symmetry and stability. Advanced structural characterization techniques, like X-ray diffraction, electron microscopy, and spectroscopy, are addressed in order to highlight the structural changes caused by the doping process. the review also analyses the dielectric properties of alkaline earth metal-doped double perovskite materials, emphasizing the changes in electrical response and polarisation behaviour caused by the dopants. The link between dopant concentration, crystal structure, and dielectric performance is studied, providing useful insights for enhancing dielectric functions. The paper additionally analyses the numerous uses of double perovskite composites in photocatalysis, solar energy conversion, and electrical devices, highlighting the potential they hold as multifunctional materials. Finally, the importance of alkaline earth metal doping in altering the structural and dielectric properties of double perovskite materials is highlighted in this comprehensive analysis. It emphasizes the bright prospects of double perovskite composites even more, making it a significant resource for academics and scientists working on functional materials, energy conversion technologies, and advanced electronic applications.

Keywords: Double perovskite; solid-state reaction; X-ray diffraction; Crystal structure; spectroscopy; dielectric properties; alkaline earth metal

Received: October 2023; Accepted: February 2024

THE REVIEW OF STRUCTURAL AND DIELECTRIC PROPERTIES OF DOUBLE PEROVSKITE MATERIALS

1. Review on Alkaline Earth Metals as Doping Materials in Structural Properties of Double Perovskite Materials

The alkaline earth elements, which include beryllium, magnesium, calcium, strontium, and barium, all having a valence-shell configuration of ns^2, are typically categorized as main-group elements and fall within the group of s-block atoms [1]. In recent decades, a number of significant research has been conducted on alkali metal tungstates with a scheelite structure, a subset of the inorganic tungstate family. The distinctive arrangement of deltahedral AO_8 (where A = Ba, Sr, Ca) and tetrahedral WO_4 symmetries in the divalent metal tungstate category has captured the interest of condensed matter physicists. This group of ceramics, denoted as AWO_4 (where A = Ca, Sr, Ba), displays exceptional stability when subjected to thermal and chemical conditions. Exploring stable crystal structures based on their chemical compositions to uncover novel physical properties has long been a focal point for materials scientists. While various combinations of elemental perovskite ceramics with specific doping ratios have been documented, the interaction between alkali/alkaline earth metals and transition elements stands out as a particularly intriguing area. Transition elements found in the periodic table exhibit captivating properties that appeal to both physicists and technologists due to their diverse and wide-ranging applications. With the growing demand for electronic devices featuring electromagnetic shielding, which captures and transforms electromagnetic energy, notably into thermal energy through smooth reflection cutoff, as well as applications in sensors, microwaves, and catalysts, a comprehensive investigation into AWO_4 ceramics has become imperative.

X-ray diffraction (XRD) data for $Nd_{2-x}Sr_xNiMnO_6$, with varying Sr concentrations (x = 0.1, 0.3)

†Paper presented at the 3rd Virtual International Symposium on Sciences (3rd VISoS 2023)

exhibit a solitary monoclinic phase within the $P2_1/n$ space group for both samples. This suggests that Sr doping up to x = 0.3 does not introduce any structural instability or phase transition [2]. Similar to other study, $La_{2-x}Sr_xNiMnO_6$ (for x = 0, 0.3, and 0.5) exclusively adopts the monoclinic $P2_1/n$ structure [3]. Furthermore, study of Sr doped at A-site of $Sm_{2-x}Sr_xNiMnO_6$ (x = 0.0, 0.2, and 0.4) [4], and $Gd_{2-x}Sr_xCoMnO_6$ (x = 0, and 0.5) [5] also exhibited a singular monoclinic structure, which could be accurately indexed using the $P2_1/n$ space group. However, from a previous study, the primary peaks of X-ray patterns for the materials $Ba_{1-x}Sr_xLa_{0.95}Eu_{0.05}MgSbO_6$ with various values of x (x = 0, 0.1, 0.3, 0.5, 0.7, 0.9, 1.0) could be attributed to a single-phase, monoclinic ($P2_1/n$) double perovskite structure of $BaLaMgSbO_6$ but a minor peak at 28.7° did not correspond to the perovskite phase. X-ray diffraction (XRD) is highly sensitive to cation ordering, which can be inferred from the presence of super-lattice reflections [6]. In anoher study, $Ba_{2-x}Sr_xZnWO_6$ compounds with the range of compositions ($0 \leq x \leq 1$) exhibited a cubic symmetry with the F*m*-3*m* space group, while the range ($1.2 \leq x < 2$) displayed a tetragonal symmetry with the I4/*m* space group. For x = 2, a monoclinic symmetry with the $P2_1/n$ space group was observed [7]. Other studies have proven that the Sr doped in $CaSrScRuO_6$ cryztallized in an orthorhombic cell with the space group *Pbnm*. The shift of peaks toward lower angles in the $CaSrScRuO_6$ compound ~~is~~ was a result of partially substituting Ca^{2+} with the larger Sr^{2+} ion [8]. However, from the diffraction patterns, the study revealed $Pr_{2-x}Sr_xFeCrO_6$ compounds (x = 0 to 1) also exhibited a crystalline nature with an orthorhombic crystal structure but with different space group which is *Pnma* [9]. Furthermore, the XRD patterns of $Pr_{2-x}Sr_xCoFeO_6$ with varying Sr doping levels (x = 0, 0.2, and 0.4) were studied, but double perovskite Pr_2CoFeO_6 is a newly discovered material for which there is no standardized XRD reference. Thus, we used the standard reference for $Pr(Co_{0.5}Fe_{0.5})O_3$ (ICSD-244742) in order to attempt to interpret the XRD patterns of Pr_2CoFeO_6. The results indicated that all diffraction peaks in the Pr_2CoFeO_6 samples matched with a typical single-phase orthorhombic *Pnma* structure [10]. Conversely, the X-ray diffraction patterns for $La_{1.5}Sr_{0.5}CoMnO_6$ and $LaSrCoMnO_6$ exhibited a coexistence of rhombohedral (with a space group of *R*3*c*) and monoclinic (space group $P2_1/n$) crystal structures [11]. On the other side, the results of the refinement process for $Ba_{2-x}Sr_xFeMoO_6$, which featured varying Sr content confirmed that all the samples possessed a cubic structure with the F*m*-3*m* space group [12]. On the other part, the room temperature of X-ray diffraction (XRD) patterns for $SrLaMnFeO_6$ demonstrated that these materials consist solely of single-phase double perovskite oxides. Further examination of the XRD data through Rietveld refinement confirmed that a rhombohedral structure with the space group *R*3*c* has been achieved [13].

In Ba-doped $Sr_{2-x}Ba_xFeMoO_6$, the length of both the a- and c-axes, and consequently the overall unit cell volume, increased as the level of Ba-doping (x) increased. The initially distorted octahedral of FeO_6 and MoO_6 approached a more symmetrical octahedral shape with increasing Ba substitution, leading to an enhancement in the crystal structure's symmetry. X-ray diffraction (XRD) patterns revealed the tetragonal (*I*4/*m*) crystal structure for $Sr_{2-x}Ba_xFeMoO_6$ [14]. Furthermore, $Ca_{1.5}Ba_{0.5}FeVO_6$ sample under investigation exhibited the lowest value of tolerance factor in the monoclinic system. As a result, it was determined that the structure of this particular sample was indeed monoclinic, $P2_1/n$ [15]. Conversely, X-ray diffraction (XRD) pattern of $Pb_{1.5}Ba_{0.5}BiNbO_6$ sample exhibited distinct, well-defined peaks, which differed from those of the individual ingredients. An attempt was made to index these peaks using various crystal systems and unit cell configurations; it was determined that the crystal system was orthorhombic [16]. However, the X-ray diffraction (XRD) pattern of $PbBaBiVO_6$ revealed several distinct diffraction peaks that were distinct from the individual components, providing evidence that the material was a single-phase compound with a monoclinic structure [17]. In the case of the double perovskite $BaKFeWO_6$, the derived t value of 0.96 signified an orthorhombic structure (F*m*-3*m*) [18]. Regarding $BaNaFeWO_6$, the calculated t value of 0.94 indicated a formation of monoclinic structural symmetry. To ensure structural stability, t must ideally lie between 0.7 and 1.0 [19]. As the tolerance factor diminishes, the lattice arrangement can shift into the rhombohedral phase (when $0.96 < t < 1$) and subsequently transition into the orthorhombic phase (for t values less than 0.96) [20]. Moreover, the introduction of K^+ and Fe^{3+} ions into the barium and molybdate positions of the host $BaMoO_4$ leads to the creation of a fresh double perovskite, $BaKFeMoO_6$. The computed tolerance factor stands at 0.9681, providing support for the emergence of a monoclinic structure [21]. In one study on the powder X-ray diffraction (XRD) patterns of the $Ba_xSr_{2-x}TiMoO_6$ ceramics confirmed that BSTM sintered samples with compositions of x = 0 and 0.1 were single-phase solid solutions. However, for $Ba_xSr_{2-x}TiMoO_6$ ceramics with x = 1.0 and 2.0 a small additional phase was present. This suggests that achieving a single-phase solid solution may not be feasible in the presence of a high concentration of barium in $Ba_xSr_{2-x}TiMoO_6$ ceramic samples. The crystal structure was refined to exhibit cubic symmetry with a P*m*-3*m* space group. [22]. In a separate study, it was observed that sharp diffraction peaks formed in all the diffraction patterns of $Ba_xSr_{2-x}FeVO_6$ (BSFV), which differed from the initial components ($BaCO_3$, $SrCO_3$, V_2O_5, and Fe_2O_3). This indicates the formation of a single-phase novel compound. The structural evolution of the BSFV(x) ceramics is closely linked to the structural tolerance factor (t). When $t > 1.05$, the structure adopts a hexagonal arrangement with *R*3*c* symmetry, while for $0.99 < t < 1.05$, a preferred cubic structure with F*m*-

3*m* space group is observed. In the range of $0.96 < t < 0.99$, the crystal structure is likely to distort into a rhombohedral system with the R3c space group [2]. Tables 1 and 2 show the overview of the refined parameters for the samples. Perovskite lattice stabilities are frequently assessed through the tolerance factor (t). For a typical perovskite structure (ABO_3), the combination of cations A and B with anion O should yield a stable perovskite structure, with the corresponding tolerance factor usually falling between 0.75 and 1.00. In the case of $La_{2-x}Sr_xNiMnO_6$ (where x = 0, 0.3, and 0.5), the calculated tolerance factors (t) are 0.971, 0.976, and 0.982, respectively. As evidenced by the tolerance factor approaching 1, substitution of Sr at the A-site in La_2NiMnO_6 enhances the compound's stability [3]. For $Pr_{2-x}Sr_xFeCrO_6$ (x = 0.00, 0.25, 0.50, 0.75, and 1.0), t values were found to be 0.8128, 0.8165, 0.8203, 0.8239, and 0.8277, respectively. These t values increased as the Sr content increased from x = 0 to 1, indicating a transition from orthorhombic (t = 0.71) to a higher value (t = 0.9). The relatively low tolerance factor of $Pr_{2-x}Sr_xFeCrO_6$ suggested that the influence of short-range trivalent metal ions like Fe^{3+} and Cr^{3+} during Sr-doping was mitigated by the presence of long-range Pr^{3+} ions, resulting in negligible lattice strain (less than unity). This estimation further confirmed significant lattice distortion in the system [9]. The study of $Ba_{1-x}Sr_xLa_{0.95}Eu_{0.05}MgSbO_6$ with various values of x (x = 0, 0.1, 0.3, 0.5, 0.7, 0.9, 1), showed that the tolerance factors (t, as defined by formula 1), continuously decreased with the introduction of smaller Sr^{2+} ions, indicating a gradual reduction in symmetry which were 0.986, 0.983, 0.977, 0.971, 0.965, 0.960, and 0.957 [6]. Conversely, the tolerance factor (t) for $SrLaMnFeO_6$ (0.996) showed that the compound was a stable perovskite material [13].

In Ba-doped $Sr_{2-x}Ba_xFeMoO_6$, the extent of anti-site defects, decreased from 30% to 20% as x increased from 0 to 0.3 [14]. The reduction in anti-site defects would likely improve the ordering of the electrical conduction layers and potentially enhances the electrical conductivity [23]. For the $Ca_{1.5}Ba_{0.5}FeVO_6$ sample under investigation, the lowest r value of 0.036 was observed in the monoclinic system. The lattice parameters associated with the monoclinic structure were determined to be a = 4.68 Å, b = 8.07 Å, c = 33.05 Å, β = 122.900, and the unit cell volume (V) was found to be 1050.81 Å³. The calculated average crystallite size (D) derived from the XRD profile was identified as 44.59 nm. This relatively small value of D can be attributed to the broadening of the XRD profile [15]. After comparing the observed and calculated tolerance factor values, it was determined that the crystal system of $Pb_{1.5}Ba_{0.5}BiNbO_6$ is orthorhombic. The unit cell parameters of $Pb_{1.5}Ba_{0.5}BiNbO_6$, refined using the least-squares method, were found to be a = 11.4515 Å, b = 12.4979 Å, c = 9.4903 Å, resulting in a unit cell volume V of 1358.19 Å³, with an estimated standard deviation of 0.0036 [16]. In a study of $PbBaBiVO_6$, it was observed that the experimental peaks conformed well to the theoretical function, resulting in a minimal goodness of fit (GOF) or $(chi)^2$ value of 1.66 within the monoclinic crystal system. In this case, the cell parameters were confirmed as a = 6.030 Å, b = 9.440 Å, and c = 12.070 Å. The corresponding reliability factors were determined as follows: $R_B(\%) = 14.80$, $R_{exp}(\%) = 24.47$, and $R_{wp}(\%) = 31.48$ [17]. The tolerance factors for $BaKFeWO_6$, $BaNaFeWO_6$, and $BaKFeMoO_6$ were calculated as τ = 2.97 [18], τ = 3.02 [19] and τ = 0.9681 [21] respectively. These values demonstrate that all these compounds are indeed double perovskite materials due to their values being less than 4.18. As the t values for the $Ba_xSr_{2-x}FeVO_6$, BSFV(x) compounds with $x = 0.0 – 2.0$ fall within the range of $1.01 \leq t \leq 1.07$, a cubic crystal structure with Fm-3m symmetry is preferred for the BSFV(x) compounds with x = 0.0–1.0. Conversely, a hexagonal structure with R3c symmetry is anticipated for the BSFV(x) compounds with x = 1.5 and 2.0 due to their t values exceeding 1.05 [2].

Upon Sr doping in $Nd_{2-x}Sr_xNiMnO_6$, slight shifts in lattice parameters were noticeable, attributed to the distinct size of Sr replacing Nd. Specifically, parameters a and c exhibited marginal increases, thereby leading to an overall volume expansion with higher Sr concentration. Conversely, parameter b experienced a reduction with Sr doping. These variations in lattice parameters can be attributed to two primary factors. The larger size of Sr compared to Nd contributes to parameter increases [2]. In $Ba_{2-x}Sr_xZnWO_6$ analysis, there are gradual decrease in cell parameters with increasing Sr^{2+} substitution, attributed to the smaller ionic radius of Sr^{2+} (1.44 Å) compared to Ba^{2+} (1.61 Å). This smaller size of Sr^{2+} leads to tetragonal and monoclinic distortions when Ba is fully substituted with Sr [7]. However, the minor changes in unit cell parameters and volume introduced by Sr doping in $La_{2-x}Sr_xNiMnO_6$ (where x = 0, 0.3, and 0.5), suggest that strontium can effectively substitute for lanthanum, without causing any structural instability or phase alteration in the original La_2NiMnO_6 structure. The substitution of Sr at the A-site in La_2NiMnO_6 enhances the compound's stability. This is attributed to the larger ionic radii of Sr^{2+} compared to La^{3+}, which contributes to the improved stability of the material [3]. On the other hand, the shift of peaks toward lower angles in the $CaSrScRuO_6$ compound is a result of partially substituting Ca^{2+} with the larger Sr^{2+} ion. Upon close examination of the X-ray diffraction profile, some weak reflections are observed, which can be attributed to the formation of small quantities of the $CaSc_2O_4$ phase. However, the refinements indicated complete anti-site disorder over the two octahedral sites, consistent with the disordered orthorhombic model. Surprisingly, there is no apparent ordering of the Ru^{5+} and Sc^{3+} cations, despite their differences in size (ionic radii are 0.565 Å for Ru^{5+} and 0.745 Å for Sc^{3+}) and

charge. In this structure, the Sc^{3+} and Ru^{5+} cations are disordered on the octahedral B-type sites, while Ca^{2+} and Sr^{2+} are disordered at the A-site, each with a coordination number of 8 [8]. Conversely, the introduction of controlled Sr substitution at the Pr-site within $Pr_{2-x}Sr_xFeCrO_6$ did not affect the crystallographic structure of the base material. The unit cell parameters in $Pr_{2-x}Sr_xFeCrO_6$ increased as the Sr content increased, given that Sr^{2+} has a larger ionic radius (1.18) than Pr^{3+} (0.99). This difference in ionic radii between Pr and Sr ions induced lattice strain, contributing to the noticeable transformation. With increasing Sr concentration, a comprehensive solid solution formed, resulting in larger crystallites [9]. Another study showeds that the introduction of Sr doping up to a concentration of x = 0.4 in $Sm_{2-x}Sr_xNiMnO_6$ did not introduce any new phases into the structure [4]. Notably, an interesting trend emerges as the Sr^{2+} content increases in $(Ba_{1-x}Sr_x)_2YSbO_6$:0.005Mn^{4+} phosphors: the diffraction peaks gradually shift to higher angles. This phenomenon can be attributed to the substitution of the larger Ba^{2+} ions (1.36 Å, CN = 6) by the smaller Sr^{2+} ions (1.13 Å, CN = 6). Both a and V exhibit linear decreases as the Sr^{2+} content increases. The reduction in a and V, respectively, signifies the incorporation of Sr^{2+} ions into the Ba_2YSbO_6 lattice through the replacement of Ba^{2+} ions [24]. Furthermore, the X-ray patterns for the materials $Ba_{1-x}Sr_xLa_{0.95}Eu_{0.05}MgSbO_6$ with various values of x (x = 0, 0.1, 0.3, 0.5, 0.7, 0.9, 1) that resulted in the strongest diffraction peaks, ranging from 31° to 32°, and gradually shifted to higher angles with increasing x, reflect the incorporation of smaller Sr^{2+} ions into the lattice. The lattice volumes gradually decreased as the Sr^{2+} concentration increased [6]. In another study of $Ba_{2-x}Sr_xFeMoO_6$ (referred to as BSFMO) samples, which featured varying Sr content, it is worth noting that a small impurity peak corresponding to $BaMoO_4$ was consistently observed in all the samples. This impurity phase, $BaMoO_4$, tends to form during the synthesis procedure. The lattice parameter decreased as the Sr concentration increased. This reduction in the lattice parameter is a direct consequence of the smaller ionic radius of Sr^{2+} (1.44 Å) in comparison to the ionic radius of Ba^{2+} (1.61 Å) [12]. In the $Gd_{2-x}Sr_xCoMnO_6$ (GCMO) sample, the structural parameters indicate a well-ordered crystal structure without any discernible splitting or tilting of the CoO_6/MnO_6 octahedra. Conversely, in the $Gd_{1.5}Sr_{0.5}CoMnO_6$ sample, structural distortions encompass unequal Co-O/Mn-O bond lengths, Co-O-Mn bond angles of less than 180°, and in-phase and anti-phase tilting of CoO_6/MnO_6 octahedra. These distortions are introduced by the substitution of an element with a different ionic radius, namely Sr^{2+}, at the Gd^{3+} site [5].

In one study of $Sr_{2-x}Ba_xFeMoO_6$, within the ab plane, the Fe–O bond length decreased, while the Mo–O bond length increased with higher x. In contrast, along the c-axis, the Fe–O bond length increased, while the Mo–O bond length decreased with Ba-doping. This means that the initially distorted octahedra of FeO_6 and MoO_6 approached a more symmetrical octahedral shape with increasing Ba substitution, leading to an enhancement in the crystal structure's symmetry [14]. In a separate study, the substitution of Ba into the A-site of the host Ca_2FeVO6 plays a substantial role in this peak broadening phenomenon. Additionally, since the sample is oxygen-rich and has undergone high-temperature calcination, there is a definite likelihood of the formation of oxygen vacancies, which also contributes to the broadening of the XRD peaks [15]. The distinctive structure of $BaKFeWO_6$ emerges from the combination of non-perovskite materials, $BaWO_4$ and $KFeO_2$, wherein K/Fe substitutions occur at the Ba/W sites in $BaWO_4$. The resultant $BaKFeWO_6$ exhibits an orthorhombic configuration with altered unit cell dimensions. While the primary peaks were clear, the presence of secondary peaks with minimal intensity, attributed to noise or background effects, was noted [18]. The X' Pert High-Score Plus software facilitated the structural analysis, with a comparison between the XRD pattern of $BaKFeMoO_6$ and non-perovskite references $BaMoO_4$ and $KFeO_2$. The consistent agreement between observed and calculated inter-planar spacing, along with minimal standard deviation of the unit cell, reinforced the monoclinic symmetry of the sample. Calculations yielded refined cell parameters, reflecting a well-correlated relationship between the stability factor and lattice parameters, thus supporting the emergence of a new polycrystalline monoclinic crystal symmetry [21]. From the powder X-ray diffraction (XRD) patterns of the $Ba_xSr_{2-x}TiMoO_6$, it can be deduced that the lattice parameter increases as the concentration of barium in $Ba_xSr_{2-x}TiMoO_6$ increases. This change is likely due to the larger size of Ba (1.35 Å) when compared to Sr (1.18 Å) [22]. In terms of distances, the V−O bond length steadily increases in the Ba-doped ceramic samples with x = 0.0–1.0, while a minor decrease is observed in the samples with x = 1.5–2.0. The Fe−O bond length, on the other hand, exhibits a general decreasing trend but with fluctuations at x = 1.50. This implies that greater structural distortion appears in the $Ba_xSr_{2-x}FeVO_6$ compounds as the Ba-doping content increases [2].

Table 1. The crystallographic data of double-perovskite materials with Sr as a doping material.

Sample	Space group	a (Å)	b (Å)	c (Å)	V (Å^3)	β (°)	R_p (%)	R_{wp} (%)	R_{exp} (%)	Source
$Nd_{1.9}Sr_{0.1}NiMnO_6$	$P2_1/n$	423656	5.471087	7.676890	227.799	90.020	22.7	14.3	10.77	[2]
$Nd_{1.7}Sr_{0.3}NiMnO_6$	$P2_1/n$	5.435216	5.459713	7.685605	228.068	90.019	27.1	16.8	12.30	
$Ba_{2.0}Sr_{0.0}ZnWO_6$	Fm-3m	8.1161			534.60		0.0835	0.125		[7]
$Ba_{1.6}Sr_{0.4}ZnWO_6$	Fm-3m	8.088			529.06		0.0769	0.113		
$Ba_{1.0}Sr_{1.0}ZnWO_6$	Fm-3m	8.035			518.75		0.0693	0.103		
$Ba_{0.8}Sr_{1.2}ZnWO_6$	I4/m	5.668		8.022	257.69		0.0752	0.111		
$Ba_{0.6}Sr_{1.4}ZnWO_6$	I4/m	5.652		8.011	255.93		0.0806	0.115		
$Ba_{0.4}Sr_{1.6}ZnWO_6$	I4/m	5.629		8.001	253.55		0.101	0.136		
$Ba_{0.2}Sr_{1.8}ZnWO_6$	I4/m	5.611		7.996	251.78		0.102	0.138		
$Ba_{0.0}Sr_{2.0}ZnWO_6$	$P2_1/n$	5.6312	5.6063	7.9222	250.10	89.958				
$La_{2.0}Sr_{0.0}NiMnO_6$	$P2_1/n$	0.54238	0.54713	0.76631	234.267	90.160	9.67	12.26		[3]
$La_{1.7}Sr_{0.3}NiMnO_6$	$P2_1/n$	5.4238	5.4713	7.6631	234.267	90.178	10.08	13.07		
$La_{1.5}Sr_{0.5}NiMnO_6$	$P2_1/n$	5.4316	5.4928	7.6913	235.865	90.181	10.54	13.56		
CaSrScRuO6	Pbnm	5.5796	5.5926	7.8988	246.48		3.19	2.45	4.27	[8]
$Pr_{2.00}Sr_{0.00}FeCrO_6$	Pbnm	5.4768	5.5409	7.7387	59.175					[9]
$Pr_{1.75}Sr_{0.25}FeCrO_6$	Pbnm	5.4792	5.5447	7.7398	60.259					
$Pr_{1.50}Sr_{0.50}FeCrO_6$	Pbnm	5.4806	5.5469	7.7406	60.284					
$Pr_{1.25}Sr_{0.75}FeCrO_6$	Pbnm	5.4824	5.5481	7.7415	60.307					
$Pr_{1.00}Sr_{1.00}FeCrO_6$	Pbnm	5.4851	5.5488	7.7428	60.315					
$Sr_2YSb_{0.995}Mn_{0.005}O_6$	Fm-3m	8.4003			592.77		5.74	8.19	5.11	[24]
$Ba_{1.0}Sr_{0.0}La_{0.95}Eu_{0.05}MgSbO_6$	$P2_1/n$	5.689	5.689	8.054	260.69	89.950	6.67	9.56		[6]
$Ba_{0.9}Sr_{0.1}La_{0.95}Eu_{0.05}MgSbO_6$	$P2_1/n$	5.687	5.693	8.047	260.57	89.900	6.57	9.15		
$Ba_{0.7}Sr_{0.3}La_{0.95}Eu_{0.05}MgSbO_6$	$P2_1/n$	5.696	5.675	8.022	259.31	89.961	5.98	8.63		
$Ba_{0.5}Sr_{0.5}La_{0.95}Eu_{0.05}MgSbO_6$	$P2_1/n$	5.664	5.675	8.020	257.83	89.878	6.87	9.73		
$Ba_{0.3}Sr_{0.7}La_{0.95}Eu_{0.05}MgSbO_6$	$P2_1/n$	5.676	5.661	8.013	255.95	89.876	7.56	10.38		
$Ba_{0.1}Sr_{0.9}La_{0.95}Eu_{0.05}MgSbO_6$	$P2_1/n$	5.669	5.672	8.002	253.14	89.895	6.89	10.08		
$Ba_{0.0}Sr_{1.0}La_{0.95}Eu_{0.05}MgSbO_6$	$P2_1/n$	5.664	5.667	7.985	252.98	89.907	7.02	9.85		

$Ba_{2.0}Sr_{0.0}FeMoO_6$	Fm-3m						16.2	12.6	8.70	[12]
$Ba_{1.9}Sr_{0.1}FeMoO_6$	Fm-3m						16.2	12.6	8.74	
$Ba_{1.8}Sr_{0.2}FeMoO_6$	Fm-3m						15.6	12.0	8.70	
$Ba_{1.7}Sr_{0.3}FeMoO_6$	Fm-3m						17.9	13.5	9.02	
$Ba_{1.6}Sr_{0.4}FeMoO_6$	Fm-3m						17.3	13.2	8.58	
$Gd_{2.0}Sr_{0.0}CoMnO_6$	$P2_1/n$	5.302	5.566	7.543		89.91				[5]
$Gd_{1.5}Sr_{0.5}CoMnO_6$	$P2_1/n$	5.379	5.425	7.633		89.85				

Table 2. The crystallographic data of double-perovskite materials with Ba as a doping material.

Sample	**Space group**	**a (Å)**	**b (Å)**	**c (Å)**	**V ($Å^3$)**	**β (°)**	**R_p (%)**	**R_{wp} (%)**	**R_{exp} (%)**	**Source**
$Sr_{1.9}Ba_{0.1}FeMoO_6$	I4/m	5.5898	5.5898	7.8965	246.740	90.0		17.63	11.10	[14]
$Sr_{1.8}Ba_{0.2}FeMoO_6$	I4/m	5.5842	5.5842	7.8964	246.244	90.0		17.28	9.82	
$Sr_{1.7}Ba_{0.3}FeMoO_6$	I4/m	5.5885	5.5885	7.9011	246.767	90.0		19.68	11.57	
$Ca_{1.5}Ba_{0.5}FeVO_6$	$P2_1/n$	4.68	8.07	33.05	1050.81	122.90				[15]
$Pb_{1.5}Ba_{0.5}BiNbO_6$	Pnma	11.4515	12.4979	9.4903	1358.19					[16]
$PbBaBiVO_6$	$P2_1/n$	6.030	9.440	12.070			14.80	31.48	24.47	[17]
$BaKFeWO_6$	Pnma	32.2059	3.8447	9.0355	270.00					[18]
$BaNaFeWO_6$	$P2_1/n$	8.4913	10.3275	6.9705	305.42	99.61	15.48	22.39	4.48	[19]
$BaKFeMoO_6$	$P2_1/n$	6.7269	4.7238	5.5255	170.24	104.160	13.4185	18.2447	3.8710	[21]
$Ba_{0.0}Sr_{2.0}TiMoO_6$	Fm-3m	3.9414	3.9414	3.9414	61.2297					[22]
$Ba_{0.1}Sr_{1.9}TiMoO_6$	Fm-3m	3.9445	3.9445	3.9445	61.3571		6.16	6.05	2.80	
$Ba_{1.0}Sr_{1.0}TiMoO_6$	Fm-3m	3.9760	3.9760	3.9760	62.8555					
$Ba_{2.0}Sr_{0.0}TiMoO_6$	Fm-3m	4.0165	4.0165	4.0165	64.7977					
$Ba_{0.0}Sr_{2.0}FeVO_6$	Fm-3m	5.628			127.03		4.636	7.198		[2]
$Ba_{0.5}Sr_{1.5}FeVO_6$	Fm-3m	5.672			129.02		4.393	8.169		
$Ba_{1.0}Sr_{1.0}FeVO_6$	Fm-3m	5.718			132.18		8.492	6.728		
$Ba_{1.5}Sr_{0.5}FeVO_6$	R3c	5.755		21.035	156.83		4.826	10.680		
$Ba_{2.0}Sr_{0.0}FeVO_6$	R3c	5.787		21.322	157.00		9.554	13.087		

2. Dielectric Properties of Double-Perovskite Materials Doped by Alkaline Earth Metals

Dielectric spectroscopy (DS) is an essential experimental technique that plays a significant role in investigating the electrical transport behaviour of materials through the analysis of dielectric phenomena as a function of frequency. It allows for the quantification of electric and dielectric properties by measuring the response of a material placed between conducting electrodes at different frequencies. DS is widely used in various fields such as materials science, physics, chemistry, colloidal science, polymers, and pharmaceutics. The examination of dielectric spectroscopy provides valuable insights into the electrical properties, transport mechanisms, and charge storage capabilities of dielectric materials. The dielectric properties are influenced by various factors, including the chemical composition and synthesis method.

The dielectric permittivity, also known as the dielectric constant, is a property used to assess a material's capacity for storing electrical charges and, consequently, the energy derived from an applied electric field. It is quantified as the ratio of the electric field strength within the material to the electric field strength in a vacuum, assuming an equal dispersion of charges [25]. In $SrCaMnTiO_6$, the dielectric constant (ε') decreases rapidly as the frequency increases, primarily due to the reduction of the space charge polarization effect. Subsequently, it remains relatively constant but increases with rising temperature at a given frequency. However, at low frequencies, the dielectric constant is notably high. This is attributed to the presence of space charge polarization at the grain boundaries, which creates a potential barrier [26]. However, the addition of (Ca, Ce) to $BiCaFeCeO_6$ has increased the dielectric constant from 400 (at 300 °C, frequency = 1 kHz) to 140×10^3. The dielectric constant rises progressively with temperature, remaining constant up to 200 °C and sharply increasing up to 300 °C, reaching a value of 300k in the frequency range of 103–106 Hz [27]. In another study, the dielectric constant (ε′) for $La_{2-x}Ca_xFeMnO_6$ within a temperature range of 303-423 K exhibited notably high dielectric constants at elevated temperatures, particularly in the lower frequency range. This phenomenon arose from the alignment of dipole moments within $La_{2-x}Ca_xFeMnO_6$ along the direction of the applied electric field [28]. The study of Sr_2CaTeO_6 revealed a significant decrease in ε' at frequencies below 100 kHz, with a reduction in the rate of decline at higher frequencies up to 1 MHz. At ambient temperature, the minimum and maximum ε' values were 6800 and 3800, respectively. With increasing temperature, the ε' values also increased [29]. Furthermore, $Sr_{2-x}Ca_xNiWO_6$ compositions exhibited a higher dielectric constant at low frequencies (1 Hz). However, with increasing frequency up to 1 MHz, the dielectric constant significantly dropped and stabilized. This behaviour is influenced by various polarization mechanisms, including ionic, dipolar, electronic, and space charge effects. At low frequencies, electric dipoles within the compounds align with the applied electric field, resulting in maximum polarization. As frequency increases, most polarizations diminish, except for electronic polarization, leading to a reduced dielectric constant [30]. Figure 1 shows the frequency dependence of dielectric constant, ε' and dielectric loss, tan δ for $Sr_{2-x}Ca_xNiWO_6$ (x = 0.00, 0.02, 0.04, 0.06). Furthermore, due to Ca substitution in $Ba_2Mg_{1-x}Ca_xWO_6$, dielectric permittivity increases with higher levels of Ca substitution. This increase can be attributed to the greater ionic polarizability of the B'-site cation (αCa^{2+} = 3.16 Å) compared to Mg^{2+} (αMg^{2+} = 1.32 Å) and the weakening of Ba–O bonds, despite an increase in cell volume with Ca substitution [31]. Moreover, $(BaSr)FeMoO_6$ dielectric constant exhibits systematic changes with temperature and frequency, it decreases as either parameter increases. This behaviour aligns with typical dielectric materials. The phenomenon is attributed to multiple types of polarization (including electronic, ionic, dipolar, and space charge polarization), which respond to changing electric fields at lower frequencies, resulting in higher dielectric constant values. However, as the frequency rises, not all polarizations can keep pace with the changing field, leading to a drop in the dielectric constant [32]. The dielectric constant of $BaLiFeWO_6$ from 25°C to 500°C showed that in the low-frequency region, a wide range of dielectric permittivity values was observed. At these temperatures, both the dielectric constant and tangent loss decreased and approached near-constant values in the high-frequency region. This behaviour suggests that in the low-frequency region, all four types of polarization contribute to the high permittivity, particularly space/interfacial polarization [25]. The dielectric constant of $BaBiLiTeO_6$ decreases as the frequency increases. This behaviour is attributed to the frequency-dependent nature of various polarization mechanisms. The overall polarization diminishes with increasing frequency, leading to a corresponding decrease in the dielectric constant. While the tested samples exhibited a high dielectric constant of approximately 30 and a relatively low dielectric loss of around 0.02 in the radio frequency region, they did not show resonance in the microwave frequency range when using the cavity method [33].

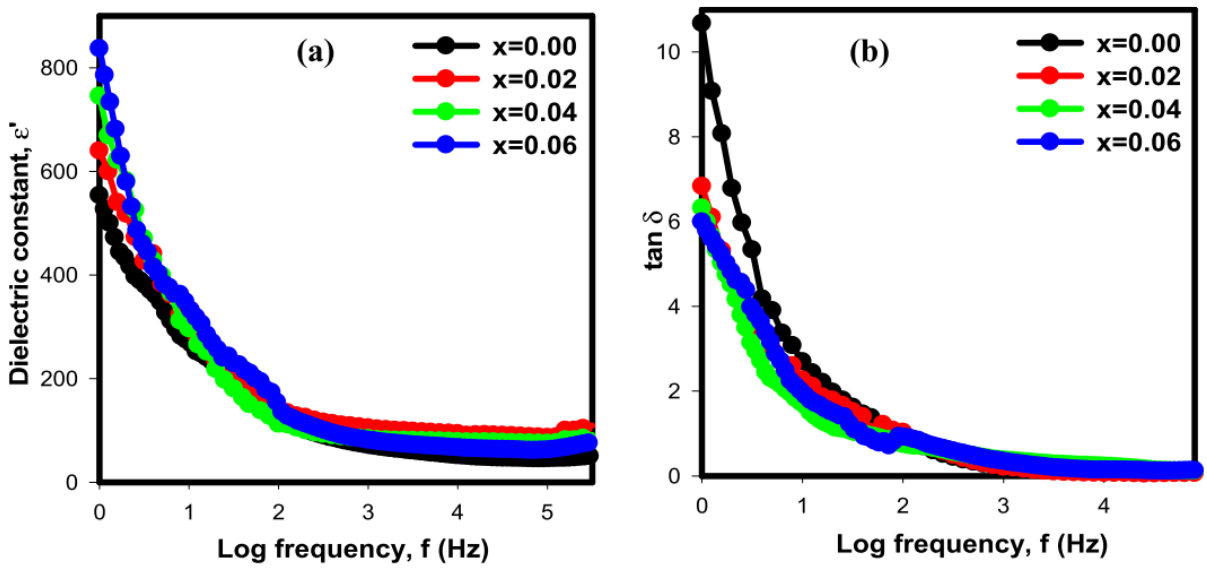

Figure 1. The frequency dependence of (a) dielectric constant, ε' and (b) dielectric loss, tan δ for $Sr_{2-x}Ca_xNiWO_6$ (x = 0.00, 0.02, 0.04, 0.06) series at room temperature in a frequency range between 1 Hz and 1 MHz [30].

The conductivity-frequency spectra of $SrCaMnTiO_6$ at room temperature proved that in the low-frequency range, grain boundaries with high resistance account for constant conductivity, while in the high-frequency range, the increase in AC conductivity is associated with grains exhibiting much higher conductivity than grain boundaries [26]. For $BiCaFeCeO_6$, the activation energy is estimated in the range of 103–106 Hz frequency and 25–300 °C temperature, with values ranging from 0.15 to 0.74 eV. These findings indicate that the conduction mechanism in the sample is primarily attributed to electron or charge carrier hopping. The conductivity increases linearly with increasing frequency. At higher frequencies, the conductivity plateau suggests DC volume conductivity, while at lower frequencies, conductivity is contact-driven [27]. The frequency-dependent behaviour of tangent loss in $La_{2-x}Ca_xFeMnO_6$ can be attributed to the conduction of charges or ions. At low frequencies, ion drift leads to fluctuations in tangent loss. At moderate frequencies, both ion jumping and conduction losses affect dielectric losses. At higher frequencies, only ion vibrations contribute to dielectric loss, resulting in frequency-independent tangent loss in this range [28]. Furthermore, the incapacity of these electric charges to readily comply with the changes in the external field may play a role in the elevated loss value. At lower frequencies, the rise in loss value with increasing temperature indicated an augmented mobility of the charge carriers, which, in turn, contributed to the enhancement of DC conductivity [29]. In $Pb_{1.5}Ca_{0.5}BiNbO_6$, where B-site cations are mainly Nb and Bi, a hopping effect occurs, resulting in a significant increase in the loss tangent and electrical conductivity. The dielectric constant (ε_r) decreases as frequency increases, which can be explained by the Maxwell–Wagner theory. For all temperatures, ε_r displays a significant dispersion at low frequencies, while at higher frequencies, it remains frequency-independent, possibly due to the absence of various polarizations [34].

Based on the studied data of $Sr_{2-x}Ca_xMnTiO_6$ and the high dielectric values, this synthesized material can be considered for use as a thermoelectric material [26]. However, the dissipation factor (tan δ) exhibits a small value at room temperature and low temperatures, suggesting potential electronic applications for $BiCaFeCeO_6$ [27]. The tangent loss (dielectric loss) in $La_{2-x}Ca_xFeMnO_6$ is high at lower frequencies and elevated temperatures but decreases as the frequency increases. This decline is due to the influence of polarization and is linked to enhanced conductivity from thermally activated charge carriers. At higher frequencies, the dielectric loss becomes almost frequency independent [28]. The tan δ values of Sr_2CaTeO_6 exhibited a temperature-dependent increase and showed a peak at lower frequencies and around 100 kHz. At the lowest frequency, the loss was 0.25, while at the highest frequency, it was 0.05 at ambient temperature. At the second peak, the loss was approximately 0.2 at ambient temperature. The high ε' values were likely a result of space charge polarization, originating from the movement of charge carriers, such as heavy electrical dipoles, associated with oxygen vacancies and defects within the grains [29]. Figure 2 shows the variation in ε' with frequencies, temperature, and variation in tan δ with frequencies of Sr_2CaTeO_6. The frequency-dependent variation in tan δ can be explained by the Maxwell–Wagner two-layer theory, suggesting that the samples of $Sr_{2-x}Ca_xNiWO_6$ are composed of two layers: grains and grain boundaries. At low frequencies, grain boundaries are more active, leading to charge carrier accumulation.

The high resistance at grain boundaries requires more energy for charge transport, resulting in high dielectric loss. In contrast, at high frequencies, grains are more active, enabling easier charge flow with minimal energy dissipation, resulting in low dielectric loss [30]. For 1:1 ordered perovskites, intrinsic dielectric loss is primarily influenced by low-frequency modes involving A-BO_6 vibrations and B-O_6 stretching vibrations. In the case of Ba_2MgWO_6 (x = 0), the over-bonded Ba–O bond contributes to its higher Q x f value compared to Sr_2MgWO_6 and Ca_2MgWO_6. The second mode is sensitive to the B'-site cation. Thus, the increased Mg/Ca–O bond strength with Ca substitution is expected to enhance the intrinsic Q x f value of $Ba_2Mg_{1-x}Ca_xWO_6$ ceramics, while the decrease in Ba–O bond strength has the opposite effect [31]. In the case of $Pb_{1.5}Ca_{0.5}BiNbO_6$, the increase in ε_r at higher temperatures is attributed to the formation of clusters and dipole ordering. Conversely, the rise in tan δ may be attributed to various factors such as lattice defects, octahedral tilting-induced disorder, and the presence of oxygen vacancies [34]. In one study of (BaSr)$FeMoO_6$, the dielectric loss (tan δ) exhibited a similar trend to the dielectric constant. At low temperatures, tan δ was relatively low, but its value increased as the temperature rose, indicating the influence of thermally induced charge carriers and defects. A broad peak in dielectric loss corresponded to a rapid decrease in the dielectric constant. As the frequency increased, this loss peak shifted to higher temperatures, suggesting thermally stimulated dielectric relaxation in these ceramics [32]. The frequency-dependent dielectric loss for the synthesized $BaLiFeWO_6$ double perovskite followed a similar trend to the dielectric permittivity. This trend persisted up to 1000 Hz, after which it became independent of frequency. High dielectric loss values at low frequencies are attributed to the misalignment of dipoles with the applied electric field. In contrast, at high frequencies, the dielectric loss decreases due to the reduced thermal agitation and misalignment [25]. The broad peaks observed in the dielectric loss of $BaBiLiTeO_6$ and $SrBiLiTeO_6$ indicated a higher dielectric loss in these materials, which explained the absence of resonance. Specifically, $BaBiLiTeO_6$ has a dielectric constant of 38 and a dielectric loss of 0.029, while $SrBiLiTeO_6$ has a dielectric constant of 30 and a dielectric loss of 0.028 at 1 MHz. The stronger ionic bonds present in the Sr compound resulted in lower polarizability, which led to $BaBiLiTeO_6$ having a higher dielectric constant compared to $SrBiLiTeO_6$ [33].

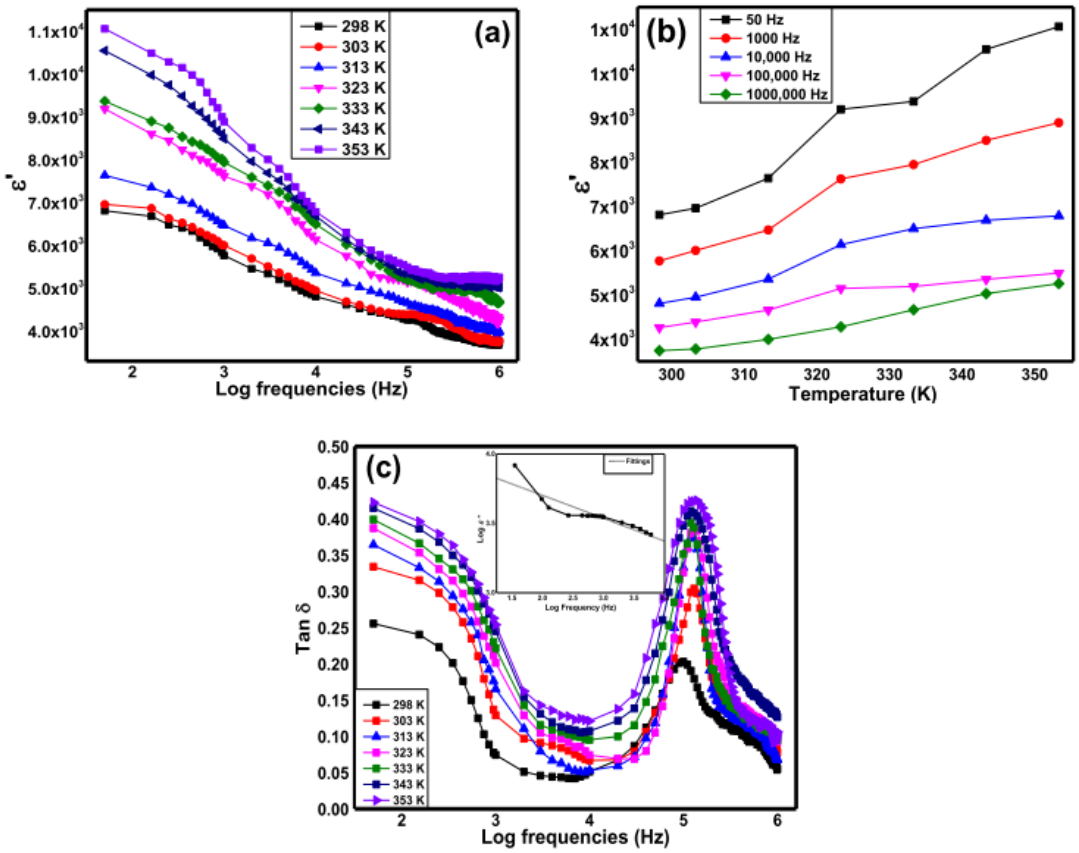

Figure 2. Variation in ε' with (a) frequencies, (b) temperature, and (c) variation in Tan δ with frequencies of Sr_2CaTeO_6 [29].

CONCLUSION

In summary, the paper demonstrates that the alkaline earth metals in these double perovskite materials generally maintain their structural stability, with only minimal lattice distortion and no phase transitions. The materials continue to exhibit complex and ordered crystal structures, making them potentially useful for various applications in materials science and technology. Furthermore, the review provides valuable insights into the dielectric behavior of various materials, shedding light on their potential applications in fields such as high dielectric materials and electronic devices. The findings highlight the importance of understanding frequency and temperature-dependent dielectric properties for designing and optimizing materials for specific applications.

ACKNOWLEDGEMENTS

We wish to convey our heartfelt appreciation to all those who have played a role in the preparation and completion of this review paper. Primarily, we want to express our gratitude to the authors of the original research papers and publications that we examined and referenced in this manuscript. Their pioneering work laid the foundation for the comprehensive analysis and synthesis we present here. This work was financially supported by FRGS grant FRGS/1/2019/STG02/UITM/02/7. Additionally, we would like to extend our thanks to Universiti Teknologi MARA for granting us access to essential resources, including research databases, and libraries. We extend our appreciation to all individuals who contributed to the development of this review paper.

REFERENCES

1. Zhou, M. and Frenking, G. (2021) Transition-metal chemistry of the heavier alkaline earth atoms Ca, Sr, and Ba. *Accounts of Chemical Research*, **54(15)**, 3071–3082.

2. Figiel, H., Zogał, O. and Yartys, V. (2005) Modifications induced in structural, electronic and dielectric properties of Nd_2NiMnO_6 double perovskite by Sr doping. *Journal of Alloys and Compounds*, **404–406**, 1.

3. Aarif Ul Islam, S. and Ikram, M. (2019) Structural stability improvement, Williamson Hall analysis and band-gap tailoring through A-site Sr doping in rare earth based double perovskite La_2NiMnO_6. *Rare Metal*, **38(9)**, 805–813.

4. Abass, S., Sultan, K., Chakravarty, S. and Choudhary, R. J. (2023) Role of structural, morphological, and electronic characteristics in investigating the low temperature transport and magnetic behavior of Sr doped Sm_2NiMnO_6. *Journal of Alloys and Compounds*, **968**, 172191.

5. Sahoo, R. C., Das, S. and Nath, T. K. (2018) Role of Gd spin ordering on magnetocaloric effect and ferromagnetism in Sr substituted Gd_2CoMnO_6 double perovskite. *Journal of Applied Physics*, **103901**, 1–8.

6. Liu, Q., Wang, L., Huang, W., Zhang, L., Yu, M. and Zhang, Q. (2017) Enhanced luminescence properties of double perovskite (Ba, Sr) $LaMgSbO_6$: Eu^{3+} phosphors based on composition modulation. *Journal of Alloys and Compounds*, **717**, 156–163.

7. Manoun, B., Ezzahi, A., Benmokhtar, S., Ider, A., Lazor, P., Bih, L. and Igartua, J. M. (2012) X-ray diffraction and Raman spectroscopy studies of temperature and composition induced phase transitions in $Ba_{2-x}Sr_xZnWO_6$ ($0 \leq x \leq 2$) double perovskite oxides. *Journal of Alloys and Compounds*, **533**, 43–52,

8. Kumar, N., Rom, T., Kumar, M., Nagaiah, T. C., Lee, E., Ham, H. C., Choi, S. H., Rayaprol, S., Siruguri, V., Mandal, T. K., Kennedy, B. J. and Paul, A. K. (2022) Unraveling the effect of A-Site Sr-doping in double perovskites $Ca_{2-x}Sr_xScRuO_6$ (x = 0 and 1): Structural interpretation and mechanistic investigations of trifunctional electrocatalytic effects. *ACS Applied Energy Materials*, **5(9)**, 11632–11645.

9. Kush, L., Srivastava, S., Vajpai, S. K. and Savilov, S. V. (2023) Effect of Sr-doping on electronic and thermal properties of $Pr_{2-x}Sr_xFeCrO_6$ ($0 \leq x \leq 1$) oxide materials synthesized by using sol-gel technique. *Journal of Asian Ceramic Societies*, **11(3)**, 300–315, 2023.

10. Wu, H., Shi, X. -L.., Liu, W. -D., Li, M., Gao, H., Zhou, W., Shao, Z., Wang, Y., Liu, Q. and Chen, Z. -G. (2021) Double perovskite Pr_2CoFeO_6 thermoelectric oxide: Roles of Sr-doping and Micro / nanostructuring. *Chemical Engineering Journal*, **425**, 130668.

11. Mandal, P. R. and Nath, T. K. (2015) Evolution of Griffith phase in hole doped double perovskite $La_{2-x}Sr_xCoMnO_6$ (x = 0.0, 0.5, and 1.0). *Materials Research Express*, **2**, 066101.

12. Hussain, I., Anwar, M. S., Khan, S. N., Shahee, A., Ur, Z. and Heun, B. (2017) Magnetocaloric effect and magnetic properties of the isovalent Sr^{2+} substituted Ba_2FeMoO_6 double perovskite. *Ceramics International*, **43(13)**, 10080–10088.

13. Brahiti, N., Abbasi Eskandari, M., Balli, M., Gauvin-Ndiaye, C., Nourafkan, R., Tremblay, A. -M. S. and Fournier, P. (2020) Analysis of the magnetic and magnetocaloric properties of $ALaFeMnO_6$ (A = Sr, Ba , and Ca) double perovskites. *Journal of Applied* Physics, **127**, 113905.

14. Habib, A. H., Saleem, A., Tomy, C. V. and

Bahadur, D. (2005) Structural, electronic, and magnetic properties of $Sr_{2-x}Ba_xFeMoO_6$ ($0 \leq x \leq 2$). *Journal of Applied Physics*, **97**, 10A906.

15. Bhattacharjee, S., Sen, S., Parida, R. K., Deb, S. K., Deb, R., Dutta, R. and Parida, B. N. (2022) Synthesis and characterization of Ba-doped Vanadium-based double perovskite for multifunctional applications. *Materials Today: Proceedings*, **57(1)**, 90–93.

16. Parida, B. N., Panda, N., Padhee, R. and Parida, R. K. (2018) Ferroelectric and optical properties of 'Ba-doped' new double perovskites. *Phase Transitions*, **91(6)**, 638–648.

17. Parida, R. K., Pattanayak, D. K., Mohanty, B., Parida, B. N. and Nayak, N. C. (2019) Dielectric and ferroelectric investigations of barium doped double perovskite Pb_2BiVO_6 for electronic and optical devices. *Materials Chemistry and Physics*, **231**, 372–381.

18. Mishra, S., Choudhary, R. N. P. and Parida, S. K. (2022) A novel double perovskite $BaKFeWO_6$: Structural, Microstructural, Dielectric and optical properties. *Inorganic Chemistry Communications*, **145**, 110068.

19. Mishra, S., Choudhary, R. N. P. and Parida, S. K. (2022) Structural, dielectric, electrical and optical properties of a double perovskite: $BaNaFeWO_6$ for some device applications. *Journal of Molecular Structure*, **1265**, 133353.

20. Amaran, N. A. and Mohamed, Z. (2021) Effect of 'A' and 'B' site substitution in Pr-based manganites: Fundamentals and main properties. *AIP Conference Proceedings*, **2720**, 040028.

21. Mishra, S., Choudhary, R. N. P. and Parida, S. K. (2023) Structural, dielectric, electric, transport, and optical properties of a double perovskite: $BaKFeMoO_6$. *Chinese Journal of Physics*, **85**, 674-691.

22. Saxena, M. and Maiti, T. (2017) Effect of Ba-doping on high temperature thermoelectric properties of Sr_2TiMoO_6 double perovskites. *Journal of Alloys and Compounds*, **710**, 472–478.

23. Heleskivi, J. and Shiosaki, T. (1976) Thermoelectric properties of EuSe. *AIP Conference Proceedings*, **29(1)**, 398–399.

24. Zhong, J., Chen, D., Yuan, S., Liu, M., Yuan, Y., Zhu, Y., Li, X. and Ji, Z. (2018) Tunable optical properties and enhanced thermal quenching of non-rare-earth double-perovskite $(Ba_{1-x}Sr_x)_2YSbO_6$: Mn^{4+} red phosphors based on composition modulation. *Inorganic Chemistry*, **57(15)**, 8978-8987.

25. Mishra, S., Choudhary, R. N. P. and Parida, S. K. (2022) Structural, dielectric, electrical and optical properties of Li/Fe modified barium tungstate double perovskite for electronic devices. *Ceramics International*, **48(12)**, 17020–17033.

26. Borole, S., Kurawle, N. and Rayaprol, S. (2023) Effect of Ca substitution on structural, magnetic and dielectric properties of Sr_2MnTiO_6 double perovskite. *Solid State Communications*, **369**, 115205.

27. Das, R. and Choudhary, R. N. P. (2019) Structural, electrical, and leakage-current characteristics of double perovskite: Sm_2CoMnO_6. *Applied Physics A: Materials Science and Processing*, **125(12)**, 231–241.

28 Ahmad, J., Yasmin, M., Ahmad, U., Hamad Bukhari, S., Nissar, U., Khan, J. A. and Abbas, H. (2021) Structural, optical, and electrical properties of alkaline earth doped $La_{2-x}A_xFeMnO_6$ (A = Ca, Sr, and Ba) double perovskites. *Journal of Nanoscope (Jn)*, **2(1)**, 69–91.

29. Halizan, M. Z. and Mohamed, Z. (2022) Dielectric, AC conductivity, and DC conductivity behaviours of Sr_2CaTeO_6 double perovskite. *Materials*, **15(12)**, 4363.

30. Mohamed Saadon, N. A. F., Taib, N. I., Loy, C. W. and Mohamed, Z. (2023) Role of Ca^{2+} doping on the enhancement of dielectric properties of $Sr_{2-x}Ca_xNiWO_6$ for energy storage device application. *Scientific Reports*, **13(1)**, 1–13.

31. Wu, J. Y. and Bian, J. J. (2012) Structure stability and microwave dielectric properties of double perovskite ceramics - $Ba_2Mg_{1-x}Ca_xWO_6$ ($0.0 \leq x \leq 0.15$). *Ceramics International*, **38(4)**, 3217–3225.

32. Barua, A., Maity, S., Kumar, S., Dutta, A. and Sinha, T. P. (2020) Structural, optical and electrical characterization of Ba_2YbTaO_6. *Physica B: Condensed Matter*, **583**, 412057.

33. Vilesh, V. L. and Subodh, G. (2018) Crystal structure, phonon modes and dielectric properties of B site ordered $ABiLiTeO_6$ (A = Ba, Sr) double perovskites. *Ceramics International*, **44(11)**, 12036–12041.

34. Parida, B. N., Biswal, P., Behera, S., Parida, R. K. and Padhee, R. (2020) Multifunctional behavior of Ca-doped niobium-based double perovskite for photovoltaic/solar cell devices. *Journal of Materials Science: Materials in Electronics*, **31(8)**, 6097–6108.